Application of the Zeeman patterns in Ov and H-alpha spectra to the local plasma diagnostics of the TRIAM-1M tokamak

Shikama, T; Kado, S; Zushi, H; Iwamae, A; Tanaka, S

PHYSICS OF PLASMAS VOLUME 11, NUMBER 10 OCTOBER 2004

Application of the Zeeman patterns in Ov and H_α spectra to the local plasma diagnostics of the TRIAM-1M tokamak

T. Shikama[a)]
Graduate School of Engineering, The University of Tokyo, 7-3-1 Hongo, Bunkyo, Tokyo 113-8656, Japan

S. Kado[b)]
High Temperature Plasma Center, The University of Tokyo, 2-11-16 Yayoi, Bunkyo, Tokyo 113-8656, Japan

H. Zushi
Advanced Fusion Research Center, Research Institute for Applied Mechanics, Kyushu University, 6-1 Kasuga-koen, Kasuga, Fukuoka 816-8580, Japan

A. Iwamae
Graduate School of Engineering, Kyoto University, Yoshida, Sakyo, Kyoto 606-8501, Japan

S. Tanaka
Graduate School of Engineering, The University of Tokyo, 7-3-1 Hongo, Bunkyo, Tokyo 113-8656, Japan

(Received 10 May 2004; accepted 23 June 2004; published online 20 September 2004)

The positions of emission of berylliumlike oxygen ions in the core region as well as the hydrogen atoms in the boundary region of the limiter shadow have been measured by means of the difference of the Zeeman patterns in the spectral shape in the poloidal section of the TRIAM-1M super conducting tokamak [H. Zushi *et al.*, Nucl. Fusion **43**, 1600 (2003)]. For determining magnetic field strength, the σ components of the Zeeman spectra are resolved by a linear polarizer. In addition to the emission region, the local hydrogen neutral temperature and the recycling flow velocity are measured in the boundary region, and the bulk ion temperature is measured in the core region.
 [DOI: 10.1063/1.1783877]

I. INTRODUCTION

In fusion-relevant magnetic confinement devices, measurement of local plasma parameters is an extremely important task in both the boundary and core regions. In the boundary region, electron temperature and density decrease rapidly over a small scale across the magnetic field lines in the scrape-off layer, and atomic and molecular processes affect the dynamic behavior of plasmas, such as the recycling processes near the first wall[1] or divertor flow reversal.[2] Therefore, it is important to measure local neutral density and flow of electrons as well as that of ions. On the other hand, in the core region, local plasma flow provides information on the radial electric field, which is important for the formation of the edge and internal transport barriers,[3] and local spectral line profiles; namely, the intensity and Doppler broadening and shift of the emission from impurity ions determine the plasma confinement characteristics.[4]

Spectrum measurement by means of standard passive spectroscopy consists of a line-integrated emission along a viewing chord. To obtain the local plasma parameters, charge exchange spectroscopy[5] using neutral beam injection (NBI) have been widely applied to the highly ionized ions in the core region. For the measurement of the low temperature neutrals and ions in the boundary region, laser-induced fluorescence[6] or plume spectroscopy[7] have been used.

In recent years, local measurements of the low temperature neutrals in the boundary region have been applied using the Zeeman effect.[8–10] When a magnetic field strength is large and has a gradient along the viewing chord, the local parameters can be measured based on the difference of the Zeeman patterns in the spectral shape using only passive spectroscopy. Even though, in principle, this method is also applicable to the high temperature ions in the core region, almost no attempts have been made because of the difficulties mentioned briefly in the following sections. The present paper demonstrates the local measurement of highly charged ions in the core region based on the Zeeman patterns, and the neutrals on the edge on limiter-shadow region.

II. METHOD

A. Calculation of the Zeeman effect

In the external magnetic field $\mathbf{B}$, the Hamiltonian for valence electrons is written as

$$\mathbf{H}_{\mathrm{tot}} = \mathbf{H}_0 + \mathbf{H}_{\mathbf{LS}} + \mathbf{H}_{\mathbf{B}} \tag{1}$$

$$= \sum_i \left\{ \frac{1}{2m_e}\left[\mathbf{p_i} - \frac{e}{c}\mathbf{A}(\mathbf{r_i})\right]^2 + \phi(\mathbf{r_i}) \right\} + \zeta \mathbf{L}\cdot\mathbf{S} + \frac{e}{2m_e}\mathbf{B}\cdot(\mathbf{L}+2\mathbf{S}), \tag{2}$$

where m_e and $\mathbf{p}$ are, respectively, the electron mass and momentum, $\mathbf{A}$ and ϕ are the vector and scalar potentials of the field, respectively, ζ value represents the strength of spin-orbit interaction, and $\mathbf{L}$ and $\mathbf{S}$ the total orbital and total spin angular momenta, respectively.

[a)]Electronic mail: shikama@flanker.q.t.u-tokyo.ac.jp
[b)]Electronic mail: kado@q.t.u-tokyo.ac.jp

The matrix elements H_{LS} and H_B are small compared to H_0 and can be treated as perturbation. The perturbation of energy level is the eigenvalue of the perturbation matrix. In the limit of a weak magnetic field ($H_B \ll H_{LS}$) or strong magnetic field ($H_B \gg H_{LS}$), diagonalization can be done analytically, and the perturbation of the energies are obtained as

$$\Delta E_{\text{Zeeman}} = \mu_B |\mathbf{B}| g_J M, \tag{3}$$

$$\Delta E_{\text{Paschen–Back}} = \mu_B |\mathbf{B}| (M_L + 2M_S), \tag{4}$$

where μ_B is the Bohr magneton, g_J the Lande's g factor, M the total magnetic quantum number which is the eigenvalue of the magnetic field directional component of the total angular momentum $\mathbf{J}(=\mathbf{L}+\mathbf{S})$, and M_L and M_S are total orbital and spin magnetic quantum numbers which are the eigenvalues of magnetic field directional components of $\mathbf{L}$ and $\mathbf{S}$, respectively. The resultant formula of the weak field case is called the normal or anomalous Zeeman effect, and the strong field case is called the Paschen–Back effect. In the case of an intermediate magnetic field ($H_B \simeq H_{LS}$), however, the perturbation of the energy level is given by numerical calculation of the secular equation. Using the quantum number (S,L,J,M) as an index of wave functions, the matrix elements of $\mathbf{H_B}$ are given as

$$\langle J,M|\mathbf{H_B}|J',M'\rangle = \sum_{M_L,M_S} (M_L + 2M_S)\mu_B|\mathbf{B}|\langle J,M|M_L,M_S\rangle \times \langle M_L,M_S|J',M'\rangle. \tag{5}$$

The wave function of the perturbed state $|\psi\rangle$ is obtained as the linear combination of the wave functions of the unperturbed states as

$$|\psi\rangle = \sum_{J,M} C_{J,M}|J,M\rangle \tag{6}$$

where $C_{J,M}$ is a constant, and the transition dipole moment between upper and lower states is given using the Wigner–Eckart theorem as

$$|\mathbf{D}|^2 = e^2|\langle\psi|\mathbf{r}_q|\psi'\rangle|^2 \tag{7}$$

$$= e^2 \left| \sum_{J,M}\sum_{J',M'} C^*_{J,M}C_{J',M'}\langle J\|\mathbf{r}\|J'\rangle \begin{pmatrix} J & 1 & J' \\ -M & q & M' \end{pmatrix} \right|^2, \tag{8}$$

where ( ) denotes the Wigner 3-j symbol, $q=M-M'$, and $q=0, \pm 1$ corresponding to the π and the $\pm\sigma$ transitions, respectively. The reduced matrix elements $\langle J\|\mathbf{r}\|J'\rangle$ can be written as

$$\langle J\|\mathbf{r}\|J'\rangle = (-1)^{S+1+L+J'}\sqrt{(2J+1)(2J'+1)} \begin{Bmatrix} L & J & S \\ J' & L' & 1 \end{Bmatrix} \times \langle L\|\mathbf{r}\|L'\rangle, \tag{9}$$

where { } denotes the Wigner 6-j symbol. Then, the intensity of the transition is obtained using upper state population n' and transition frequency ν as

$$I \propto n'\nu^4|\mathbf{D}|^2. \tag{10}$$

Thus the relative transition probabilities among different ΔJ transitions can be calculated. The upper state population n' is assumed to be statistically populated and proportional to the degeneracy $2J+1$.[11]

B. Application to the core plasmas

The line emission from the core region originates mainly from the impurity ions. Compared to the emission from the low temperature neutrals, the Doppler broadening effect on the spectral shape becomes larger. Wavelength broadening evaluated as the full width at half maximum due to the Doppler effect is written as

$$\Delta\lambda_{\text{Doppler}} = 2\sqrt{\ln 2}\sqrt{\frac{2k_BT}{m}\left(\frac{\lambda_0}{c}\right)^2}, \tag{11}$$

where T and m are the temperature and mass of the ion, respectively, λ_0 the vacuum wavelength of the emission without the Doppler effect, k_B the Boltzmann constant, and c the light velocity, while the shift of transition energy due to the Zeeman effect can be roughly estimated by Eq. (3) as $\Delta E \simeq \mu_B|\mathbf{B}|$ and with the aid of the relationship between energy and wavelength shift

$$\Delta E \simeq \frac{hc}{\lambda_0^2}\Delta\lambda, \tag{12}$$

where h is the Plank constant. The wavelength shift due to the Zeeman effect is estimated as

$$\Delta\lambda_{\text{Zeeman}} \simeq \frac{\lambda_0^2}{hc}\mu_B|\mathbf{B}|. \tag{13}$$

Then, the magnetic field strength which equalizes the magnitudes of both effects is evaluated as

$$|\mathbf{B}| = 1.65\times10^{-6}\times\frac{1}{\lambda_0}\sqrt{\frac{T}{A}}\,[\mathbf{T}], \tag{14}$$

where A is an atomic mass number, λ is in meter and T in eV, respectively. The shorter wavelength and the larger ratio of T/A give the larger magnetic field strength required for the measurement of the Zeeman effect. In the core region, the wavelengths of the brightest emission lines from the highly ionized impurity ions are in the ultraviolet region and higher magnetic field strength is required compared with the emissions in the near-infrared region from the low temperature neutrals. We applied the following three assumptions in order to overcome this drawback.

First, in the core plasmas, the positions of the ion line emissions are a function of the magnetic flux surfaces, because the plasma parameters on the same magnetic flux surface are constant. Thus, we can assume that the ions in the high-field and low-field sides along the viewing chord have the same temperature and emission intensity. Second, because the wavelength shift of the π components is not sensitive to magnetic field strength, only the σ components were observed to allow clear observation of the Zeeman pattern.

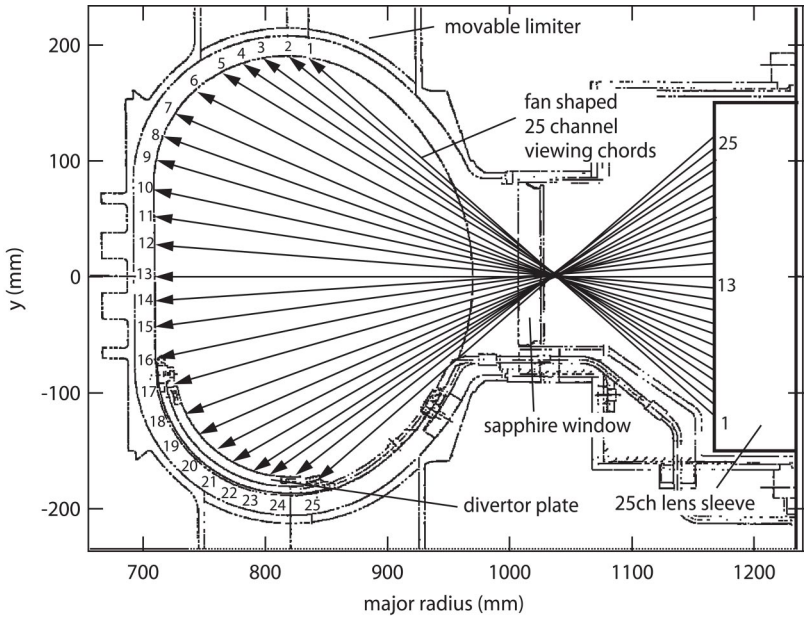

FIG. 1. Schematic of the TRIAM-1M poloidal section and 25 fan-shaped viewing chords. Emissions from the plasmas are collected using 25-channel quartz lenses through a sapphire window. The upper and lower viewing chords (channel 1–5, and channel 17–25) observe the vacuum vessel, while the horizontal viewing chords (channel 6–16) observe the viewing dump.

The π components were eliminated using the linear polarizer. Finally, lines to be observed were selected considering that the higher A decreases the Doppler broadening and that the emission tends to localize on the specific flux surfaces depending on the charge state Z.

For applying the second method, the magnetic field pitch angle should be small enough to sufficiently quench the π components from both the high-field and low-field sides. In our case, because of the strong toroidal field and small plasma current, the pitch angle in the emission region is quite small (roughly estimated as less than ±1°) and the method is applicable for the separation of the σ components. In a more general case having a larger pitch angle, polarization-sensitive spectroscopy would be required.

In the core region of the TRIAM-1M tokamak, easily observable impurity emission lines are Cv ($1s2s^3S$-$1s2p^3P$) of 227 nm and Ov ($2s3s^3S$-$2s3p^3P$) of 279 nm. Assuming that the ion temperatures are ionization energies, which are 392 eV and 114 eV, respectively, the calculated magnetic field strengths from Eq. (14) are 41 T and 15 T, and are reduced by half to 20.5 T and 7.5 T by using the only $\pm\sigma$ components. The wavelength shift of the $\pm\sigma$ components are approximated as the same in opposite wavelength directions, thus the required magnetic field strength is reduced by half. Therefore, under the experimental condition of $B=6-7$ T, the Ov ion becomes a candidate for measurements.

III. EXPERIMENTAL SETUP

The experiments were performed in the superconducting tokamak TRIAM-1M[12] under the condition of 8.2 GHz lower hybrid current driven (LHCD). The maximum magnetic field strength of 8 T is generated by 16 Nb_3Sn super conducting toroidal field coils. The plasma boundary shape is restricted by three D-shaped poloidal limiters and one vertically movable limiter installed in the upper port of the vacuum vessel. In the present paper, all experiments were performed in the limiter configuration.

An arrangement of 25 fan-shaped viewing chords in the poloidal cross section is shown in Fig. 1. The upper and lower viewing chords (channel 1–5 and channel 17–25) observe the vacuum vessel, while the rest of the chords (channel 6–16) observe the viewing dump for Thomson scattering. The upper and lower viewing chords collect the emissions from roughly a single magnetic field position, while the horizontal viewing chords collect the line-integrated emissions originating from two different magnetic field positions which are in the high-field and low-field sides of the torus plasma.

Emissions from the plasmas were collected using 25 channel lens sleeves through a sapphire window. Each sleeve, separated by 10 mm in pitch, is equipped with a quartz collimator lens having a focal length of 8 mm and a diameter of 5 mm. In front of each lens sleeve, a linear polarizer is attached with its polarization axis perpendicular to the direction of the toroidal field for the observation of the σ components. The collected emissions were transferred to a spectrometer using a 12 m bundled quartz optical fiber having a core diameter of 230 μm and a clad diameter of 250 μm. The spectrometer (Acton Research AM-510) having a focal length of 1 m and equipped with a 1800 grooves/mm ruled grating was used. The Princeton Instruments ICCD-1024MG-E/1 consisted of water-cooled and front-illuminated charge coupled device (CCD), and an image intensifier was used for the detector. The CCD dimension was 1024×256 pixels with each pixel size of 26×26 μm^2. The 256 pixels were binned by 7 pixels into 25 channels corresponding to the 25 viewing chords. The A/D conversion rate in the CCD chip was 100 kHz and the resolution was 14 bit. A typical condition of the measurements was a slit width of 40 μm and a microchannel plate gain of 5% of the hardware maximum gain. The reciprocal linear dispersion was 0.0115 nm/pixel at 558 nm and 0.0106 nm/pixel at 656 nm, and the wavelength resolution was $\Delta\lambda_{inst} \simeq 0.025$ nm. Due to the weak emission intensity and the signal amplitude noise in the image intensifier, the time resolu-

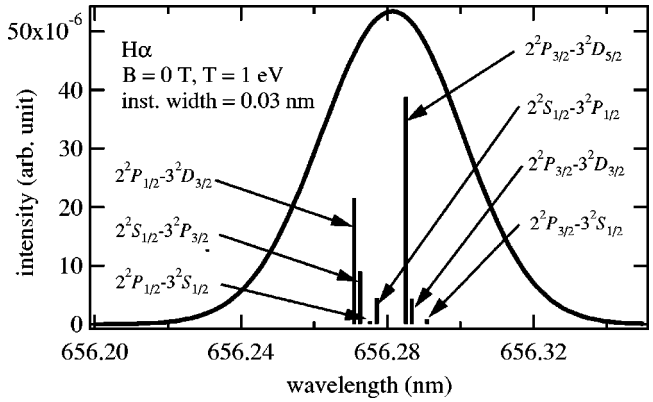

FIG. 2. Calculated H_α spectrum using a temperature of 1 eV and an instrumental width of 0.03 nm. Without an external magnetic field, the spectrum consisted of seven fine structure transitions, and the spectral shape is not Gaussian.

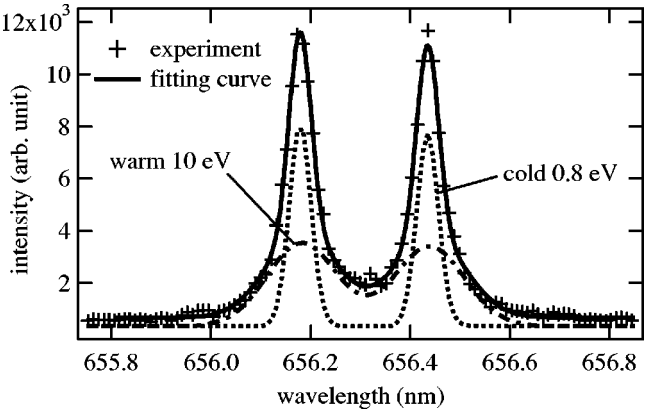

FIG. 4. Measured H_α spectrum along the peripheral viewing chord (channel 2) and fitting results assuming single magnetic field. The hot temperature component is not apparent and fitting can be done with the cold (0.8 eV) and warm (10 eV) temperature components.

tion was about 2 s for the H_α case and 5 s for the Ov case.

IV. HYDROGEN SPECTRA IN THE BOUNDARY REGION

A. Modeling of the H_α line shape

The H_α spectra were observed in the 8.2 GHz LHCD plasmas. The toroidal magnetic field strength was 7 T at the major radius of $R=800$ mm, the plasma current was 40 kA, and the line-averaged electron density was 1×10^{19} m^{-3}. The H_α spectrum consisted of seven transitions due to the fine structure splitting as shown in Fig. 2. In the external magnetic field, these seven components split into a total of 18 π and 30 σ components. When analyzing the emission from the low temperature neutrals, one should estimate the exact shape of the H_α spectrum containing these transitions, because the shape of the spectrum is strongly affected by fine structures. In the fitting procedure, the 30 σ components were calculated using the quantum mechanical calculation written in Sec. II. An example of the calculated σ components of H_α spectrum at a magnetic field strength of 7 T are shown in Fig. 3.

In addition to the effects of fine structures, one should consider the multitemperature components of hydrogen atoms, which are produced through atomic and molecular processes in the boundary region. When not taking the vibrational excitation of hydrogen molecules into consideration, temperatures of hydrogen atoms in the boundary region can be roughly classified into three categories,[13,14] cold (0–1 eV), warm (1–10 eV), and hot (~50 eV) components. As listed in Ref. 15, the possible processes which produce cold and warm components are dissociation from the hydrogen molecules and hydrogen molecular ions with the average kinetic energy of 0.3 and 1.5 eV for the cold components and 7.0 eV for the warm components. However, it should be noted that when hydrogen molecules are vibrationally excited, the average kinetic energy of dissociated atoms is broadened.[16] On the other hand, the hot components are produced mainly by the atoms reflected from the first wall[17] and the charge exchange neutrals $H^+ + H \rightarrow H + H^+$.[14]

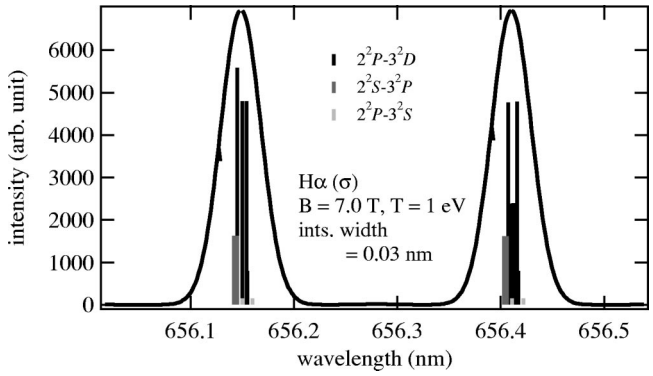

FIG. 3. Calculated σ components of the H_α spectrum in the case of $B=7$ T.

Using the spectra observed in the upper and lower viewing chords, a fitting procedure assuming a single magnetic field and three temperature components were applied. As can be seen in Fig. 4, the hot temperature component is not apparent, so that fitting was performed for the two temperature components, i.e., cold and warm. In order to determine more detailed temperature components, further investigation such as calculation using the neutral transport code will be required. Since the objective of this paper is mainly local measurement of the emission, two temperature components were *a priori* assumed in the fitting procedure for the H_α spectra.

B. Magnetic field measurements

The fitting function consists of the two Gaussian components at the two magnetic field positions, which correspond to the emissions from the high-field and low-field sides, and a background level. The two Gaussian components in each side are represented by six independent parameters of two temperatures, two peak intensities, and two central wavelengths. Then, the total number of fitting parameters were 15. The spectrum observed in the near horizontal viewing chord (channel 12) and its fitting results are shown in Fig. 5.

As seen in the raw data, two peaks are observed in the shorter wavelength σ component, indicating that the line consists of emission from the high-field and low-field sides.

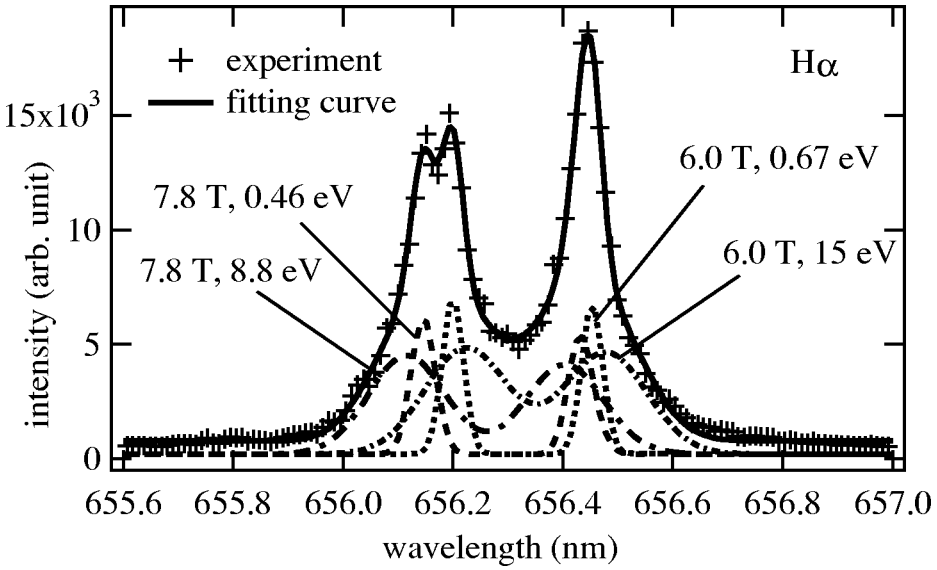

FIG. 5. H_α spectrum observed along the horizontal viewing chord (channel 12) and fitting results assuming two magnetic fields and two temperature components. From the raw data, two peaks are observed on the shorter wavelength σ component which indicates that the line integration of the emission originated from the high-field and low-field sides. The two magnetic field positions of 7.8 T and 6.0 T are separated.

The dotted line shows the fitted results of two temperature components at the two magnetic field positions. In this case, two magnetic field positions of 7.8 T and 6.0 T are separated. Figure 6 shows the separated positions of the emissions. Filled circles indicate the separated positions of emissions along the viewing chords, while marker size represents the relative intensity of the cold component. The horizontal bar shown with the marker is the standard deviation of the fitting procedure. Filled triangles denote the positions obtained on the peripheral viewing chords assuming a single magnetic field for checking the results based on the two temperature fittings. The dotted line shows the position of the last closed flux surface. Emissions in the high-field side originate from the region between the vacuum vessel and the D-shaped poloidal limiter surface, namely, the so-called limiter shadow which indicates the area between the vacuum vessel and the limiter surface as depicted by the bold lines in Fig. 6. This is because plasma is attached to the inboard side of the limiter surface. Under our present condition, the expected difference of the magnetic field strengths between the high-field and low-field sides are less than 2 T based on the Eq. (14). When the difference of the magnetic field strength becomes less than ~1.5 T, the Zeeman split and the Doppler broadening of the cold components become comparable. Therefore, on the viewing chords between the central and peripheral regions, misfitting due to the mixing of the small Zeeman split and the broadening of the cold and warm temperature components occur; these data points are shown by open circles in Fig. 6. However, the obtained emission positions in the central and peripheral regions, which are indicated by filled circles and filled triangles, are consistent with the bright positions in the visible video image measured by the TV camera. The camera shows the poloidal cross section of the torus for the purpose of monitoring the plasma position.[12]

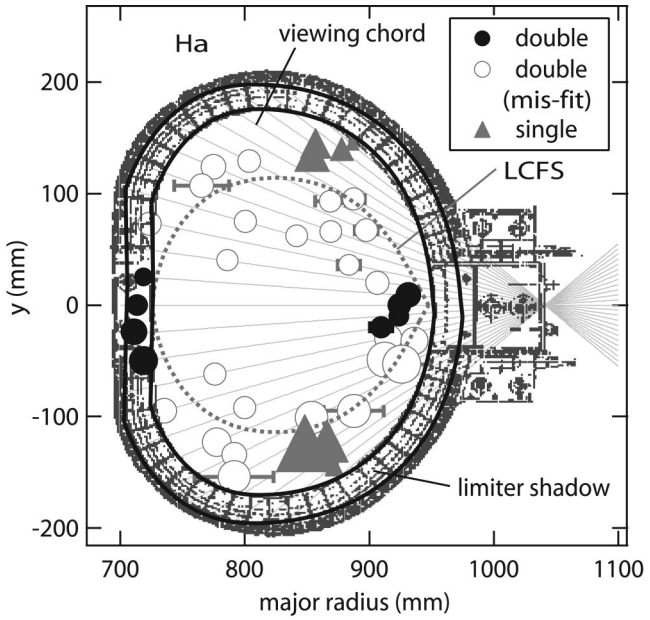

FIG. 6. Obtained positions of H_α emission. Filled circles denote the separated positions of emission, and marker size represents the relative intensity of cold components. The horizontal bar shown with the marker is the standard deviation of the fitting procedure. Filled triangles denote the positions obtained on the peripheral viewing chords using a fitting procedure that assumes a single magnetic field. The dotted line shows the position of last closed flux surface (LCFS). On the viewing chords between the central and peripheral regions, misfitting due to the mixing of the small Zeeman split and the broadening of the cold and warm temperature components occur; these data points are denoted by open circles.

C. Flow measurements

The flow velocity of hydrogen atoms was estimated based on the Doppler shift of the separated spectra. The relative Doppler shift was measured using the difference of the central wavelengths between the high-field and low-field sides, due to the lack of an absolute wavelength reference. In Fig. 5, it can be observed from the shape of the spectrum that the central wavelength of the cold components in the high-field side are blueshifted compared to that in the low-field side because only the shorter wavelength part of the σ components separate into two peaks. Thus, the flow of the cold

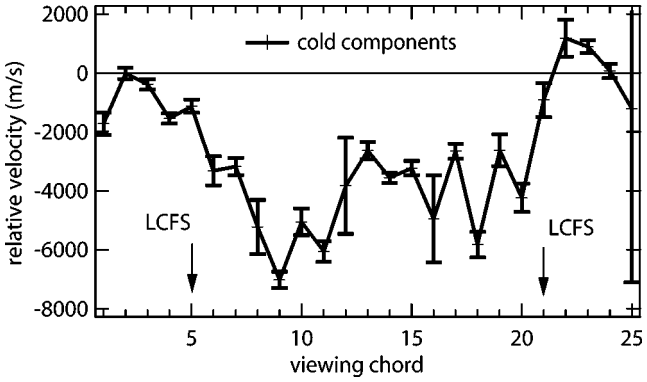

FIG. 7. Averaged relative flow velocities of cold components with respect to the viewing direction. LCFS corresponds to channel 5 and channel 21 as shown in Fig. 6.

components can be interpreted as directing from the first wall to the core region. From the fitting results, the averaged relative flow velocity of the cold components are measured as shown in Fig. 7. Because of the fan shape of the viewing chords, the direction of flow is not apparent in the peripheral region; however, in the central chords the averaged relative flow velocity was estimated at about 4 km/s. For the warm components, an inward flow of about 20 km/s was also observed in the central chords. However, the fitting error is comparable to the absolute values so that reliability in the current measurement system is not sufficient. This point will be investigated in the future.

V. Ov SPECTRA IN THE CORE REGION

A. Fitting procedure

For application to the core region, Ov ($2s3s^3S_1$-$2s3p^3P_1$) of 278.7 nm transition was observed. The experiment was performed in the 8.2 GHz LHCD plasmas with electron cyclotron heating. The toroidal magnetic field strength was 6.4 T, the plasma current was 40 kA, and the line-averaged electron density was 1.4×10^{19} m^{-3}. The second-order diffraction spectrum was measured for higher resolution. The Ov $2s3s^3S_1$-$2s3p^3P_1$ transition contains three π and four σ components, and using the linear polarizer, only the σ components were clearly observed, as shown in Fig. 8.

Compared with the H_α emission which originates in the boundary region, the difference of magnetic field strength between the two emission positions in the high-field and low-field sides becomes smaller. Thus, in addition to the first assumption written in Sec. II B, which is reasonable in the light impurity ion case, the Doppler shift of the spectra was neglected in the fitting procedure for reducing the free parameters. In fact, the poloidal flow of Ov ions was driven dominantly by the $\mathbf{E}\times\mathbf{B}$ drift, so that the flow velocity become quite small (less than 1 km/s) under the condition of a large magnetic field strength of 6.4 T with a typical radial electric field of several kV/m. For the measurements of such a small flow velocity, higher resolution optics is required.

Concerning the assumption written in Sec. II B, first, the Doppler broadening of the Ov ions on the magnetic flux surface was determined. The fitting procedure under the assumption of a single magnetic field was applied to the spectrum measured on the outermost viewing chord in which Ov emissions can be observed (channel 17, $\rho=0.7-0.8$). The Ov ion temperature on the magnetic flux surface was deduced to 70 eV (the fitting error is less than ±4 eV) as can be seen in Fig. 9. Although the discharge condition is not the same, similar bulk ion temperature of 100–200 eV can be observed using a neutral particle analyzer.[18] From this result, the temperature of 70 eV was used as a fixed value over the identical flux surface in all fitting procedures.

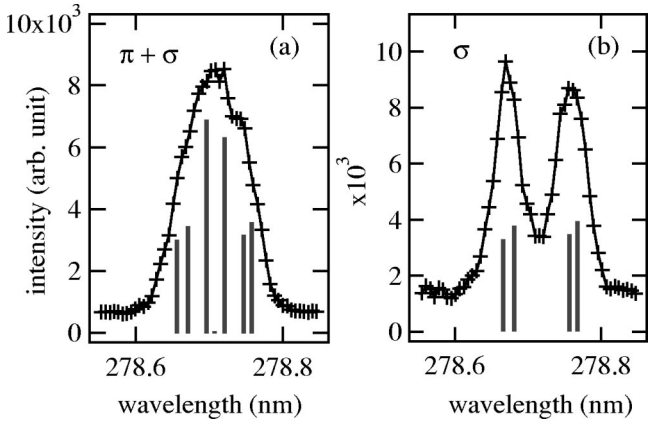

FIG. 8. Measured Ov $2s3s^3S_1$-$2s3p^3P_1$ second-order diffraction spectrum and calculation results of $B=7$ T (stick to zero lines). (a) Without the polarizer. Both the π and σ components are observed. (b) Using the polarizer. The π components are quenched and only the σ components are clearly observed.

B. Magnetic field measurements

The number of fitting parameters is reduced to a total of five in this case; i.e., the single Gaussian components at the two magnetic field positions and a background level. The single component in both sides have the same intensity and the same temperature. The spectrum observed in the near horizontal viewing chord (channel 11) and its fitting results are shown in Fig. 10. The dotted line shows the fitting results of two magnetic field positions, 6.9 T and 5.7 T. The sepa-

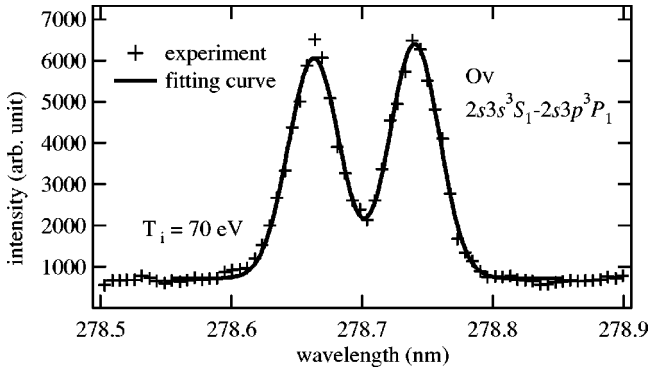

FIG. 9. Measured Ov $2s3s^3S_1$-$2s3p^3P_1$ second-order diffraction spectrum along the peripheral viewing chord (channel 17) and fitting results assuming a single magnetic field. An ion temperature of 70 eV was fitted with high accuracy, and this value was used as a fixed ion temperature on the magnetic flux surface.

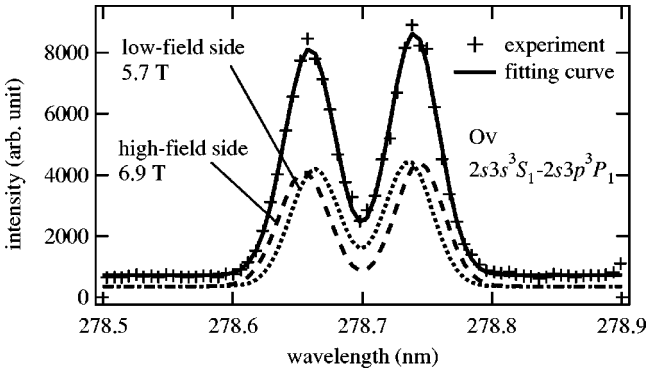

FIG. 10. Ov $2s3s^3S_1$-$2s3p^3P_1$ second-order diffraction spectrum observed along the horizontal viewing chord (channel 11) and fitting results assuming two magnetic field strength positions and an ion temperature of 70 eV. Two magnetic field positions of 6.9 T in the high-field side and 5.7 T in the low-field side are separated using the fitting procedure.

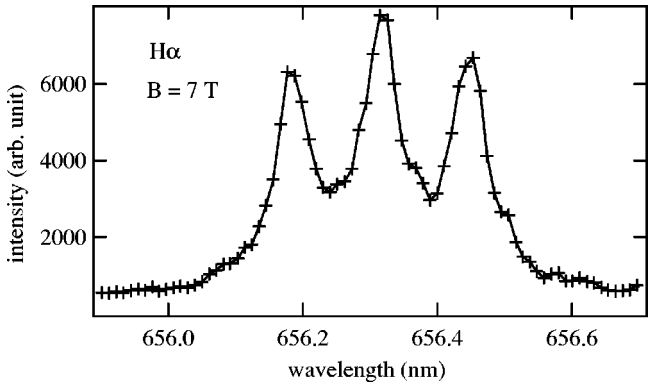

FIG. 12. H_α spectrum measured without the linear polarizer under an experimental condition of B=7 T. The spectral width of the π and σ cold components seems to be almost same.

rated emission positions are shown in Fig. 11. The meaning of the markers are the same as the H_α case. The dotted line shows the magnetic flux surfaces in the core region, while the solid line shows the peak position of the emission profile obtained by the Abel inversion.[19] In the core region, the shape of the magnetic flux surface is almost axially symmetrical, and the spatially symmetrical emission was observed on the CCD image. Thus, in the Abel inversion, an axially symmetrical emission was assumed for the first-order approximation. In this case, the normal distance from the plasma center to the viewing chords can be treated as an observation using parallel viewing chords. The measured

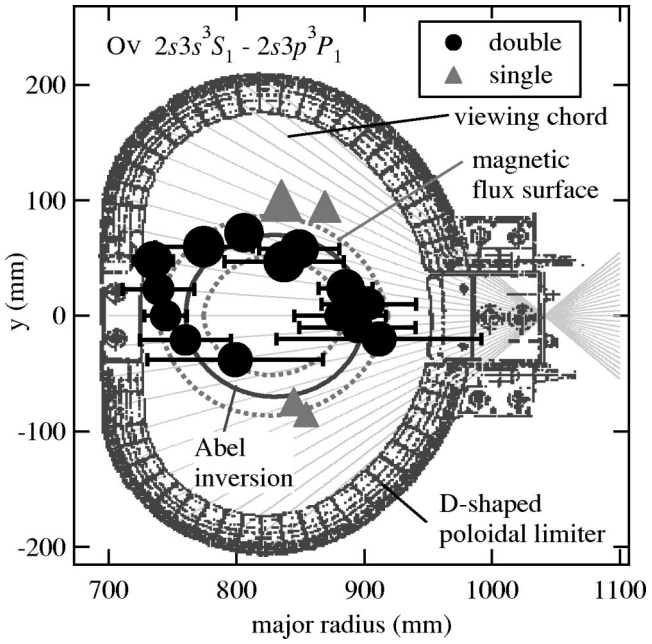

FIG. 11. Obtained positions of Ov $2s3s^3S_1$-$2s3p^3P_1$ emission. The meanings of the markers are the same as those in Fig. 6. The dotted line shows the position of the magnetic flux surfaces in the core region, and the solid line shows the peak position of the emission profile obtained by the Abel inversion assuming axially symmetrical emission.

emission positions lay along the magnetic flux surfaces within error bars and the results are consistent with those of the Abel inversion.

VI. DISCUSSION

In the present paper, the emission region should be sufficiently localized in the viewing chord in order to allow the reconstruction procedure from the observation of a well-defined Zeeman pattern and to reduce the error of the fitting procedure. It is possible to evaluate the localization of the emission by observing the π and σ components separately and comparing the width of the spectra, since only σ components are broadened due to the integration of the Zeeman shift over the emission region.

In the case of H_α, the measured spectrum without the linear polarizer is shown in Fig. 12. This figure shows that the widths of the π and σ cold components are almost the same. This indicates that as long as the cold components are concerned, the region of emission can be regarded as sufficiently localized.

As for the Ov, from Fig. 9 the spectrum observed in the peripheral region can be fitted with high accuracy using the fitting procedure assuming a single magnetic field position. This result suggests that even if there is some broadening of the emission region, its effect on the spectral shape is small.

When applied to bulk ion temperature measurement in the core region, Ov ions should be thermalized with the bulk ions. In the core region of the TRIAM-1M tokamak, the ionization and thermalization times of the Ov ions with the bulk hydrogen ions are the same order of about 200–500 μs. Therefore, the approximation of thermal equilibrium is roughly correct, and the obtained Ov ion temperature can be regarded as that of the bulk ions. On the other hand, in the fitting procedure, we made some assumptions for compensating the smaller magnetic field differences between the high-field and low-field sides in the small tokamak. However, in larger devices such as the International Thermonuclear Experimental Reactor (ITER), the magnetic field differences become larger and the difficulties can be reduced. Furthermore, in plasmas with high electron temperatures and density gradients, emission lines from impurity ions will be sharply

localized and one can determine the emission positions more precisely. In this case, the ion temperature may be determined from the central chord alone. Thus, especially when the viewing chord is restricted and the Abel inversion cannot be applied, this method provides an efficient tool to determine the local value of the ion temperature and plasma flow.

VII. SUMMARY AND CONCLUSIONS

The measurement of local plasma parameters by means of the Zeeman effect was applied to the boundary and core regions of the TRIAM-1M tokamak, and the applicability of the measurement to the core plasmas was demonstrated. For determining the Zeeman effect exactly, quantum mechanical calculation was performed as a fitting procedure, and to allow a clear observation of the Zeeman pattern, only σ components of the spectrum were measured using the linear polarizer.

The H_α spectra were observed in the boundary region and the obtained emission positions showed results consistent with the TV camera image. From the Doppler profile of the spectra, cold temperature components of less than 1 eV and the warm temperature components of about 10 eV were observed, and the recycling fluxes directed from the first wall to the core region with the flow velocities of $4-20$ km/s were observed for the cold and warm components, respectively.

In the core region, the Ov $2s3s^3S_1$-$2s3p^3P_1$ second-order diffraction spectra were measured. In order to overcome the difficulties related to the observed Zeeman patterns, the assumption that the emission of the Ov ions becomes a function of the magnetic flux surface was applied in the fitting procedure. The obtained emission positions lay along the magnetic flux surface and are consistent with the results of the Abel inversion. The bulk ion temperature near $\rho=0.7 \sim 0.8$ (more precisely corresponding to the peak position of Abel profile) was estimated as 70 eV from the measured Ov lines. The applicability of this method can be expanded by selecting other lines localized in different regions. Moreover, this method is more easily and effectively applied to larger devices.

ACKNOWLEDGMENTS

The support of the staff of the TRIAM-1M experimental group is gratefully acknowledged. The authors also acknowledge Dr. Motoshi Goto of the National Institute of Fusion Science for his help of making the calculation code of the Zeeman effect.

This work was partly supported by the Japan Society for the Promotion Science, by a Grand-in-Aid for Scientific Research from the Ministry of Education, Culture, Sports, Science, and Technology of Japan, and by the collaboration program of the Research Institute for Applied Mechanics (Advanced Fusion Research Center) of Kyushu University.

[1] R. Monk, A. Loarte, A. Chankin *et al.*, J. Nucl. Mater. **241–243**, 396 (1997).
[2] J. Boedo, G. Porter, M. Schaffer *et al.*, Phys. Plasmas **5**, 4305 (1998).
[3] T. Hahm, Plasma Phys. Controlled Fusion **44**, A87 (2002).
[4] R. Groebner, Phys. Fluids B **5**, 2343 (1993).
[5] R. Isler, Plasma Phys. Controlled Fusion **36**, 171 (1994).
[6] K. Muraoka and M. Maeda, Plasma Phys. Controlled Fusion **35**, 633 (1993).
[7] B. LaBombard, S. Gangadhara, B. Lipschultz, and C. Pitcher, J. Nucl. Mater. **313**, 995 (2003).
[8] J. Weaver, B. Welch, H. Griem *et al.*, Rev. Sci. Instrum. **71**, 1664 (2001).
[9] B. Welch, J. Weaver, H. Griem, W. Noonan, J. Terry, B. Lipschultz, and C. Pitcher, Phys. Plasmas **8**, 1253 (2001).
[10] M. Goto and S. Morita, Phys. Rev. E **65**, 026401 (2002).
[11] A. Blom and C. Jupén, Plasma Phys. Controlled Fusion **44**, 1229 (2002).
[12] H. Zushi, S. Itoh, K. Hanada *et al.*, Nucl. Fusion **43**, 1600 (2003).
[13] U. Samm, P. Bogen, H. Hartwig *et al.*, J. Nucl. Mater. **162–164**, 24 (1989).
[14] B. Wan, J. Li, J. Luo, J. Xie, Z. Wu, and X. Zhang, Nucl. Fusion **39**, 1865 (1999).
[15] H. Kubo, H. Takenaga, T. Sugie, S. Higashijima, S. Suzuki, A. Sakasai, and N. Hosogane, Plasma Phys. Controlled Fusion **40**, 1115 (1998).
[16] S. Tanaka, B. Xiao, K. Kobayashi, and M. Morita, Plasma Phys. Controlled Fusion **42**, 1091 (2002).
[17] R. Aratari and W. Eckstein, Nucl. Instrum. Methods Phys. Res. B **42**, 11 (1989).
[18] H. Zushi, K. Nakamura, S. Itoh *et al.*, Nucl. Fusion **39**, 1955 (1999).
[19] P. Vicharelli and W. Lapatovich, Appl. Phys. Lett. **50**, 557 (1987).